RESEARCH ARTICLE

Bridging the Urban Canopy Sublayer to Aerodynamic Parameters of the Atmospheric Surface Layer

Qi Li[1] · **Gabriel Katul**[2]

Abstract

Within the roughness sublayer (RSL) of dense urban canopies composed of uniformly distributed cuboids, the time and planar-averaged mean velocity profile exhibits an approximate exponential shape characterized by a depth-independent attenuation coefficient a. A formulation that links a to the zero-plane displacement d and aerodynamic roughness length z_{om} is proposed using a one-dimensional momentum balance between the background mean horizontal pressure gradient, vertical gradients of total stresses, and the drag force. Dispersive effects on a within the urban RSL are then explored using large-eddy simulations (LESs) that vary independently the planar (λ_p) and frontal (λ_f) densities of the cuboids. The LES results are used to compute d and z_{om} by fitting a log-profile to the mean velocity above the canopy. Within the canopy, the LES results are also used to estimate (i) a by fitting an exponential profile to the computed time and planar-averaged velocity, (ii) profiles of drag coefficients, and (iii) turbulent as well as dispersive stresses. The LES results demonstrate that dispersive stresses can be commensurate with turbulent stresses in magnitude and act in the same direction. Moreover, dispersive transport, determined from vertical gradients of dispersive stresses, is some 25–75% of turbulent stress gradients. These dispersive effects impact a (and thus d and z_{om}) via two mechanisms: (i) reducing the effective adjustment length scale that leads to an increase in a and (ii) increasing the effective mixing length that leads to a reduction in a across a wide range of λ_f and λ_p. These two effects are shown to be partly compensatory giving rise to an apparent constant a with respect to height inside the canopy. The effects of mean recirculation and the usage of the drag force centroid method to estimate d are discussed. The analysis also evaluates the consequences of a finite roughness sublayer thickness extending above the canopy on the derived expressions.

Keywords Dispersive stresses · Large-eddy simulations · Urban canopy turbulence · Velocity attenuation coefficient

✉ Qi Li
   ql56@cornell.edu

1   School of Civil and Environmental Engineering, Cornell University, Ithaca, NY, USA

2   Department of Civil and Environmental Engineering, Duke University, Durham, NC, USA

1 Introduction

The underlying surface of a typical urban environment is characterized by roughness elements such as buildings and houses. These elements are commonly represented as bluff-body obstacles (e.g. sharp-edged cuboids) that interact with a turbulent airflow. This interaction plays out in three regions of the atmospheric boundary layer (ABL): the urban canopy sublayer (CSL), roughness sublayer (RSL) and the inertial sublayer (ISL). The CSL is pragmatically defined as the layer from the ground all the way to the roof or building top embedded within the roughness sublayer (Rotach 1999; Christen et al. 2009). The RSL typically extends from two to five times of the CSL depth (Cheng and Castro 2002), where the flow is still being influenced by individual roughness elements. The ISL is above the RSL and usually spans up to 10–20% of the ABL depth. The mean velocity profile within the neutral ISL is reasonably approximated by the log-law (Pope 2000). The presence of roughness elements is 'sensed' within the ISL through aerodynamic parameters such as the aerodynamic roughness length z_{om} and a zero-plane displacement d. Deriving z_{om} and d from obstacle properties and their layout continues to draw research attention given the immediate need in numerical weather predictions, climate models, and large-scale air quality models (Rotach 1999; Grimmond and Oke 1999; Grimmond 2006; Britter and Hanna 2003; Coceal and Belcher 2004; Fernando et al. 2010). Beyond z_{om} and d, there is a growing need for detailed representation of the urban CSL in mesoscale models (Martilli et al. 2002; Nazarian et al. 2020). One of the challenges in representing the urban CSL is related to the presence of significant dispersive stresses, which arise from the spatial correlation of time averaged three-dimensional velocities. Transport of the mean momentum can be augmented by the presence of strong dispersive stresses (Poggi and Katul 2008; Cheng and Castro 2002; Li and Bou-Zeid 2019). For this reason, the dependence of dispersive stresses on different surface morphologies is being evaluated (Moriwaki and Kanda 2006; Giometto et al. 2016; Li and Bou-Zeid 2019) and some closure strategies for dispersive stresses are beginning to permeate operational models (Nazarian et al. 2020). Yet, how dispersive stresses in the CSL are linked to the ISL aerodynamic parameters remains unanswered.

A convenient starting point is to consider a high Reynolds number flow within and above uniformly distributed obstacles (cuboids) covering a flat surface. The flow is assumed to be stationary and planar homogeneous in the absence of subsidence. The flow is driven by a background kinematic mean pressure gradient $(dP/dx)_b$ that is resisted by a drag force F_d exerted by the obstacles on the flow and the ability of turbulence to transport momentum from various layers in the atmosphere towards zones experiencing momentum deficit. For this idealized set-up, the temporally and planar-averaged mean momentum balance reduces to

$$0 = -\left(\frac{dP}{dx}\right)_b + \frac{d\tau}{dz} - F_d(z), \tag{1}$$

where z is the vertical direction with $z = 0$ set at the ground surface, x is the longitudinal direction, $F_d(z)$ is the kinematic drag force acting on the flow and includes form drag arising from pressure drop across obstacles and viscous stresses acting on the surface area of the obstacles, and τ is the total kinematic stress given by

$$\tau = \tau_t + \tau_d = -\left[\langle\overline{u'w'}\rangle + \langle\overline{u}''\overline{w}''\rangle\right], \tag{2}$$

where τ_t and τ_d are the turbulent $\langle\overline{u'w'}\rangle$ and dispersive $\langle\overline{u}''\overline{w}''\rangle$ stresses, respectively, w and u are the vertical and horizontal velocity components acting along z and x, respectively, overline is time averaging, $< . >$ is planar averaging, primed quantities are deviations from

their time-averaged state, and double-primed quantities are deviations from their planar-averaged state. The viscous stress contribution to τ is ignored relative to τ_t given the high Reynolds number flow assumption. In canopy flows, $< . >$ is commonly applied to a thin elemental volume of thickness dz set at height z. The planar extent of the averaging volume is presumed to be sufficiently large to include a number of canopy elements but not so large so as to encompass planar variability in canopy area density (Finnigan 2000). Conservation laws applied to the fluid part necessitate that the elemental volume averaging be conducted across the fluid volume only (also known as intrinsic averaging) whereas averaging over the total elemental volume (also known as extrinsic or superficial averaging) is routinely used when representing the canopy as a homogeneous porous medium (Schmid et al. 2019; Böhm et al. 2013). The two volume averages are related to each other by the canopy porosity $1 - \phi_s$, where ϕ_s is the fractional solid volume. Differences in the rules for averaging arise when ϕ_s is varying on the planar scale of the averaging volume. The case to be explored here considers a repeating array of elements so that the averaging volume is unambiguous (intrinsic) and taken to be a repeating unit. Even within a restricted scope of idealized averaging volume, stationary and planar homogeneous flow at high Reynolds number, how to represent τ_t, τ_d and F_d as a function of temporally and planar-averaged flow statistics for various arrangements of cuboids so as to derive z_{om} and d in the ISL remains a daunting challenge.

For the flow within the CSL, a number of assumptions are routinely invoked to arrive at expressions for z_{om} and d including (i) closing $\langle u'w' \rangle$ using a turbulent viscosity characterized by a mixing length l_m, which may not be a constant and given by (Coceal and Belcher 2004)

$$\tau_t = l_m^2 \left(\frac{dU}{dz} \right)^2, \tag{3}$$

(ii) $|\tau_d/\tau_t| \ll 1$ (Coceal and Belcher 2004; Yang et al. 2016; Macdonald et al. 1998), and (iii) adopting a quadratic drag-law for F_d given by

$$F_d(z) = \frac{1}{2} c_d a_s U(z)^2 = \frac{U(z)^2}{L_c}, \tag{4}$$

where the wind speed $U(z) = < \overline{u} >$ is used for notational convenience, and $c_d(z)$ is a dimensionless local (or sectional) drag coefficient. Although $c_d(z)$ can vary at least by an order of magnitude across different urban geometries (Coceal et al. 2006; Leonardi and Castro 2010), in several simplified models (Coceal and Belcher 2004; Yang et al. 2016), it is often set as constant of order unity. Here, a_s is the canopy frontal area per unit air volume obstructing the flow, and $L_c = 2(c_d a_s)^{-1}$ is the adjustment length scale (Belcher et al. 2003), which characterizes the distance over which boundary-layer flow adjusts to the canopy roughness elements until a local balance between the downward transport of momentum by turbulent stresses and removal of momentum by the drag of canopy elements is attained. An alternative interpretation, which is more pertinent here, is that L_c measures how quickly the turbulent kinetic energy in eddies (k) advecting at $U(z)$ is dissipated by the work to overcome drag elements. In this interpretation, it is assumed that the relaxation time $\tau_\epsilon = k/W_d$, where $W_d = (1/2)(c_d a_s)U(z)k$ is the work done by turbulence to overcome the drag by the obstacles and produce wakes, and $L_c = \tau_\epsilon U(z)$ (Finnigan 2000; Poggi et al. 2009). A smoothly varying drag-force requires large separation between the size of the roughness elements and the canopy size itself. In vegetated canopies, this scale separation is likely to hold as large separation between canopy height and leaf or stem dimensions exists. For this reason, the approximation of a high Reynolds number porous medium flow with $\phi_s \ll 1$ holds for vegetated canopies (Finnigan 2000). In urban canopies, this assumption may not hold.

Accepting momentarily all these assumptions yield an exponential $U(z)$ profile as a solution to Eq. 1 as first proposed for agricultural crops (Inoue 1963). An exponentially shaped $U(z)$ profile was reported by a number of experiments and simulations across a variety of urban and vegetated roughness configurations in the CSL (Macdonald et al. 1998; Coceal and Belcher 2004; Yang et al. 2016). However, significant deviations from an exponential $U(z)$ profile as well as concerns about the validity of all three aforementioned assumptions have been reported and discussed elsewhere (Castro 2017). Thus, the first motivation here is to examine how different arrangements of the same cuboid elements distort the exponential shape of $U(z)$. The second is to explore whether and how these distortions may be related to τ_d and c_d (or a combination thereof). In particular, bluff obstructions such as cuboids tend to generate a momentum deficit region behind them that impacts both c_d and τ_d. While a number of studies did report $|\tau_d/\tau_t| < 0.1$ for dense slender rod canopies, those findings do not hold for their sparser rod densities counterparts where $|\tau_d/\tau_t| \sim 0.3$ (Poggi et al. 2004b; Poggi and Katul 2008). For cuboid objects, τ_d was shown to be large in magnitude (Kanda et al. 2004; Li and Bou-Zeid 2019; Blunn et al. 2021), but may or may not act in the same direction as τ_t (Poggi and Katul 2008; Böhm et al. 2013; Blunn et al. 2021). The third is to link the aforementioned two effects to the two aerodynamic parameters z_{om} and d. Towards this end, published large-eddy simulation (LES) runs across different arrangements of cuboids (Li et al. 2020) are analysed. These arrangements cover slender obstructions (small a_s) where large channelling is allowed, wide obstructions (large a_s), and symmetric arrangements. The work here is primarily diagnostic but necessary to transition towards a future prognostic framework of representing these CSL effects on d and z_{om}.

2 Method

The repeating unit forming the obstacles to be analysed is described elsewhere (Li et al. 2020) but is reviewed for completeness. In a planar area A_t, the repeating unit is characterized by dimensions D_x (along x) and D_y (along the lateral direction y) with $D_x = D_y$ and $A_t = D_x D_y$. Within this repeating unit, a cuboid with constant height h, width L_{yb} and length L_{xb} is placed where L_{yb} need *not* be identical to L_{xb}. The distances between adjacent cuboids are defined by W_{xb} (along x) and W_{yb} along y. Hence, $D_x = L_{xb} + W_{sb}$, $D_y = L_{yb} + W_{yb}$. For a constant h, three-dimensional parameters are commonly used to characterize the canopy morphology (hereafter labelled as morphological parameters): the fractional solid volume ϕ_s, the frontal area index λ_f, and planar area index λ_p are defined by:

$$\phi_s = \frac{L_{xb} L_{yb} h}{A_t h} = \frac{L_{xb} L_{yb}}{A_t}, \tag{5}$$

$$\lambda_f = \frac{L_{yb} h}{A_t} = \phi_s \left(\frac{h}{L_{xb}} \right), \tag{6}$$

$$\lambda_p = \frac{L_{xb} L_{yb}}{A_t} = \phi_s. \tag{7}$$

In the case of cubes, $L_{xb} = h$ and $\lambda_f = \lambda_p$. Since L_{xb} need not be identical to L_{yb} or h, λ_f and λ_p by design can be made to vary independently. As before, the fractional volume occupied by air in the CSL is $1 - \phi_s$ and the canopy area density can be defined as the frontal area per unit volume of air in the CSL (i.e. intrinsic) given as

$$a_s = \frac{L_{yb} h}{A_t h (1 - \phi_s)} = \frac{1}{h} \frac{\lambda_f}{1 - \lambda_p}. \tag{8}$$

While in vegetated canopies $\phi_s \ll 1$ (Finnigan 2000), ϕ_s can be as large as 0.5 in urban canopies. With this definition for a_s, the normalized adjustment length scale can be related to the two morphological parameters and c_d using

$$\frac{L_c}{h} = \frac{2}{c_d} \frac{(1 - \lambda_p)}{\lambda_f}. \tag{9}$$

When c_d is a constant independent of z (commonly assumed to be around unity in analytical models), L_c/h is uniquely described by morphological parameters. It should be pointed out that a number of LES studies have already discussed non-uniform heights of roughness elements (Yang et al. 2016) on RSL flow statistics, especially in real urban canopies characterized by $\lambda_p > 0.3$ (Cheng and Castro 2002; Kanda et al. 2013; Yoshida et al. 2018). Hence, the work here is restricted to the independent variation of λ_p and λ_f at constant h/H, where H is the domain height. This restriction forms a logical starting point to address the goals here but certainly does not offer a complete view of how urban morphological parameters impact momentum transport in the CSL.

2.1 Flow Within the Inertial Sublayer

To define a aerodynamic roughness length and a zero-plane displacement, it is necessary to assume that the mean velocity profile in the ISL (i.e. $z/h \geq 1$) is given by

$$U(z) = \frac{u_\tau}{\kappa} \ln\left(\frac{z - d}{z_{om}}\right), \tag{10}$$

where $\kappa = 0.4$ is the von Kármán constant and u_τ is the friction velocity (here related to the background kinematic mean pressure gradient as given by $u_\tau^2/\rho\delta$). The wake-function correction introduced by others (Yang et al. 2016) has been ignored here, but they can be incorporated should the need arise. Their incorporation requires the inclusion of the boundary-layer height as an additional length scale. Also, the flow is assumed to be neutrally stratified and no stability correction functions are included so that the mixing length l_m for $z/h \geq 1$ is given by $l_m = \kappa(z - d)$. Different derivations (e.g. Macdonald et al. 1998; Kanda et al. 2013; Yang et al. 2016) linking z_{om} and d to obstacle properties and their layout (e.g. λ_f, λ_p, c_d) require models for the mean flow within the CSL.

2.2 Flow Within the Urban Canopy Sublayer

Assuming $|\tau_d/\tau_t| \ll 1$ and combining Eqs. 3 and 4 with Eq. 1 for $z/h \leq 1$ results in

$$\frac{d}{dz}\left[l_m^2\left(\frac{dU}{dz}\right)^2\right] = F_d + \left(\frac{1}{\rho}\frac{dP}{dx}\right)_b = \frac{U^2}{L_c} + \left(\frac{1}{\rho}\frac{dP}{dx}\right)_b. \tag{11}$$

Even for constant l_m and L_c, Eq. 11 is a nonlinear and nonhomogeneous ordinary differential equation that is difficult to solve. The nonhomogeneity arises from an externally imposed finite but constant background mean pressure gradient, which is not small in many LES studies (Li et al. 2020). However, this equation can be transformed into an equation that is third-order, nonlinear and homogeneous by differentiating Eq. 11 with respect to z so as to eliminate the background pressure gradient. Hence,

$$\frac{d^2}{dz^2}\left[l_m^2\left(\frac{dU}{dz}\right)^2\right] = \frac{d}{dz}\left(\frac{U^2}{L_c}\right). \tag{12}$$

It can be readily verified that (Inoue 1963)

$$U(z) = U_h \exp\left[-a\left(1 - \frac{z}{h}\right)\right],$$ (13)

remains a solution to Eq. 12 where $U_h = U(h)$ and a is the attenuation coefficient given by

$$a = \left[\frac{1}{2}\frac{h}{L_c}\frac{h^2}{l_m^2}\right]^{1/3}.$$ (14)

Note that Eq. 13 is a solution of Eq. 12 *only* if a, l_m and L_c are *all* assumed not to be a function of z. If such an assumption is made, then it also follows that constant l_m and L_c imply that a is a constant and is independent of z (Coceal and Belcher 2004). If one further assumes $l_m/h = \kappa(1 - d/h)$ so as to match the CSL and ISL mixing lengths at $z/h = 1$ (i.e. l_m is continuous but need not be necessarily smooth at $z/h = 1$), Eq. 14 becomes

$$a = \left[\frac{c_d\lambda_f}{4(1 - \lambda_p)}\right]^{1/3}[\kappa(z_d)]^{-2/3},$$ (15)

where $z_d = (1 - d/h)$ is the dimensionless zero-plane displacement referenced to the canopy top. It should be further noted that the matching assumption given the above amounts to a statement that the mixing length throughout $z < h$ is constant (equal to its value $l_m/h = \kappa(1 - d/h)$ at $z = h$). In some applications, z_d may be related (but not identical) to the eddy-penetration depth, which is defined as the distance between the top of the canopy and the point within the canopy for the Reynolds stress decaying to 10% of its maximum value, as discussed elsewhere (Poggi et al. 2009; Nepf and Vivoni 2000). Whether the matching of mixing lengths occurs at $z/h = 1$ or higher up ($z/h > 1$) depends on how far the roughness sublayer extends above the CSL. The reason the RSL extends above the CSL is due to the relative contributions of the mixing layer eddies above and beyond the attached eddies to the zero-plane displacement around $z/h = 1$. For flows in a dense vegetated canopy, a mixing-layer analogy is invoked as turbulent coherent eddies resemble many aspects of flows in a mixing layer (Raupach et al. 1996). This analogy stems from the fact that flow within roughness elements is finite but slow due to obstructions whereas flow above roughness elements is unobstructed and fast thereby creating a free shear layer between them. The generation of coherent eddies of the Kelvin–Helmholtz type is dependent on the instability of this layer as dictated by the curvature of the mean velocity profile. When connecting the logarithmic and exponential mean velocity profiles at $z/h = 1$ here, mixing-layer eddies are expected to arise. This can be demonstrated by noting that as $z/h \to 1$ from the ISL and CSL sides, the associated curvatures in $U(z)$ are given by

$$\text{ISL}: \left.\frac{d^2U}{dz^2}\right|_h = -\frac{u_\tau}{h^2\kappa}\frac{1}{z_d^2} < 0,$$ (16)

$$\text{CSL}: \left.\frac{d^2U}{dz^2}\right|_h = \frac{a^2}{h^2}U_h > 0.$$ (17)

Hence, a $d^2U/dz^2 = 0$ must be crossed as $U(z)$ switches from logarithmic shape ($d^2U/dz^2 < 0$) to exponential shape ($d^2U/dz^2 > 0$). Rayleigh's point-of-inflection theorem states that $U(z)$ is inviscidly unstable and characterized by a shear length scale $L_s = [U_h/(dU/dz)|_h] = h/a$ describing the fastest growing instability mode (and hence the mixing-length properties in the CSL) as discussed elsewhere (Raupach et al. 1996; Finnigan 2000). This condition is necessary but not sufficient for the occurrence of instability (Kelvin–Helmholtz type). Flume experiments using densely arrayed rod canopies suggest that mixing-layer eddies can

contribute up to 30–40% to turbulent momentum fluxes whereas attached eddies contribute some 60–70% at $z/h = 1$ (Poggi et al. 2004c).

Moving towards the lower boundary condition, for $l_m \propto L_s$ not to be impacted by the presence of the ground (i.e. deep canopy) requires that $h/L_s > 1$ or $a > 1$. It can be conjectured that for $a > 1$, the exponential mean velocity profile is at best an acceptable descriptor of $U(z)$, at least in the upper part of the canopy for dense canopies. While the RSL can extend above the CSL (Raupach 1981), it was ignored in many urban canopy turbulence studies (Yang et al. 2016). Its inclusion requires the presence of an intermediate region so that U gradually transitions from its exponential (in the CSL) to its log-shape (in the ISL). Hence, matching the two velocity profiles at a single point set as $z/h = 1$ must be viewed as a mathematical convenience. The consequences on the attenuation coefficient a and aerodynamic parameters of transitioning from the CSL to the ISL at a preset single point $z/h = 1$ are discussed in Sect. 4.

2.3 Modelling d and z_{om}

To determine d and z_{om}, a common approach is to assume d is situated at the centroid of $F_d(z)$ (Jackson 1981; Kanda et al. 2004; Yang et al. 2016). This approximation is routinely employed in closure models of the vegetated CSL (Finnigan and Belcher 2004; Katul et al. 2004; Poggi et al. 2004a, c; Juang et al. 2008). Assuming that an exponential mean velocity profile exists for $0 < z < h$ and L_c being constant, d is linked to the attenuation coefficient a using (Jackson 1981)

$$d = \frac{\int_0^h z F_d(z) dz}{\int_0^h F_d(z) dz}, \tag{18}$$

yielding

$$\frac{d}{h} = \frac{1}{1 - \exp(-2a)} - \frac{1}{2a}. \tag{19}$$

When $a \geq 1$, $\exp(-2a) \ll 1$ and

$$\frac{d}{h} = 1 - \frac{1}{2a} = 1 - \frac{1}{2} \frac{L_s}{h}. \tag{20}$$

That is, the centroid of the drag force estimate of d yields a unique relation between the displacement height and the attenuation coefficient a (or the shear length scale L_s). With a deep canopy requiring $a \geq 1$, $d/h \geq 1/2$. As $d/h \to 1$, $L_s \to 0$ and the existence of mixing-layer eddies must now be questioned as already found in a number of simulation studies (Kanda et al. 2004; Xu et al. 2021). These studies have also criticized the use of Eq. 18 for estimating d because of recirculation patterns within the CSL (Kanda et al. 2004). For densely packed cubical obstacles, d is underestimated using Eq. 18 as discussed elsewhere (Xu et al. 2021) (see their Fig. 7). A rationale for this underestimation is that only the top part of the roughness elements interacts with the boundary layer formed above the crest of the obstacles and depth-integration across all h is questionable.

Interestingly, the estimate $z_d = 1 - (d/h) \approx (1/2)a^{-1}$ can be combined with Eq. 14 to yield

$$a = 4 \left(\frac{c_d}{\kappa^2} \right) \frac{\lambda_f}{1 - \lambda_p} = \frac{8}{\kappa^2} \frac{h}{L_c}. \tag{21}$$

This finding recovers the approximate linear relation between a and λ_f reported in experiments for inline cubes (i.e. $a = 9.6\lambda_f$) at constant λ_p (Macdonald et al. 1998). Hence, a may

be linked to c_d, λ_f, and λ_p only when d can be estimated separately (e.g. centroid method). Another common estimate of the zero-plane displacement is the empirical relation between λ_p and d given by (Macdonald et al. 1998; Coceal and Belcher 2004)

$$\frac{d}{h} = 1 + A^{-\lambda_p} \left(\lambda_p - 1 \right), \tag{22}$$

where $A \approx 4$ is an empirical constant. This relation is featured here because it offers a compact summary of a number of experiments (Macdonald et al. 1998) and simulations (Kanda et al. 2004) though the latter study set A as high as 10.

To determine z_{om}, continuity for U is enforced at $z/h = 1$. The assumption made here is that the inertial sublayer with a logarithmic U extends from $z/h = 1$ (Yang et al. 2016), and it amounts to a zero-depth RSL. Relaxation of this assumption is examined in Sect. 4. Apart from the continuity for U being enforced, a smoothness condition on U is also considered (i.e. continuity for $\mathrm{d}U/\mathrm{d}z$ or the turbulent stress). These two conditions lead to

$$\frac{z_{om}}{h} = z_d \exp\left[-\left(\frac{a}{16} z_d \right)^{-1/3} \right] = z_d \exp\left[-\left(\frac{1}{2\kappa^2} \frac{h}{L_c} z_d \right)^{-1/3} \right]. \tag{23}$$

Interestingly, the first equality in Eq. 23 can be combined with the drag force centroid estimate $z_d = (1/2)a^{-1}$ to yield $z_{om}(h - d)^{-1} \approx 0.04$. Such a small $z_{om}(h - d)^{-1} \approx 0.04$ already foreshadows issues with the drag force centroid estimate of z_d when used to infer z_{om}/h. To sum up, Eqs. 19, 21, and 23 enable the determination of the attenuation coefficient a, d/h and z_{om}/h from λ_f, λ_p, and c_d. When compared to other studies (Yang et al. 2016), the addition of a smoothness condition on U at $z/h = 1$ provides an extra relation that determines u_τ/U_h as a function of a given by

$$\frac{u_\tau}{U_h} = z_d \, \kappa \, a \approx \frac{\kappa}{2}. \tag{24}$$

This smoothness condition was not considered in prior studies (Yang et al. 2016) except indirectly through a modification to κ (Coceal and Belcher 2004). One objection to using a smoothness condition on U at $z/h = 1$ is that l_m, while continuous at $z/h = 1$, is not smooth. To be clear, smoothness in U guarantees continuity but not necessarily smoothness in τ_t. Thus, smoothness in U does not require smoothness in l_m at $z/h = 1$. Again, the first equality in Eq. 23 does not require a drag-force centroid assumption for d/h and thus forms a basis for a direct testing of extending the RSL beyond $z/h > 1$. However, the second equality in Eq. 23 employs Eq. 15 and thus is only applicable when using $z_d = (2a)^{-1}$ as derived from the centroid method for $a > 1$. Experiments and simulations for dense vegetated canopies report $u_\tau/U_h \approx 0.3$ (Raupach et al. 1996) whereas for densely arrayed rod canopies, $u_\tau/U_h \approx 0.26$ (Poggi et al. 2004c). In field and laboratory studies (both wind tunnels and flumes), u_τ/U_h is also shown to be roughly constant for dense canopies. Returning to modifications to κ (Coceal and Belcher 2004) at $z/h = 1$, one possibility is to revise l_m as $l_m/h = (\kappa/\beta)z_d$ with $\beta \approx 0.7$ to recover prior results for canopy flows. Thus, $\beta \neq 1$ may be used to directly assess the effects of a RSL extending above $z/h = 1$ and indirectly estimates contributions of mixing-layer eddies above and beyond attached eddies to momentum fluxes at $z/h = 1$. The smoothness condition resulting in Eq. 24 also provides an estimate of a depth-integrated bulk drag coefficient for dense canopies

$$C_{d,b} = \frac{u_\tau^2}{\frac{1}{2} U_h^2} = 2 \left(z_d \, \kappa \, a \right)^2 \approx \frac{\kappa^2}{2}. \tag{25}$$

Because the attenuation coefficient a varies with L_c, the first equality in Eq. 25 can also be used to link the sectional drag coefficient (i.e. c_d) to commonly used depth-integrated bulk drag coefficient in operational models after adjusting for the planar to frontal areas (Macdonald et al. 1998) as discussed elsewhere (Coceal and Belcher 2004). Again, the centroid method estimate of $z_d = (2a)^{-1}$ yields a constant $C_{d,b} = 0.08$, a low value for densely arrayed cubes. To sum up, the onset of an exponential mean velocity profile with a near-constant attenuation coefficient a does not necessarily imply all the assumptions leading to the exponential velocity profile are individually satisfied.

3 Results

The results section seeks to address the three objectives: (i) The occurrence of an exponential shape of $U(z)$ profile and deviations from it; (ii) assumptions leading to an exponential $U(z)$ with a focus on mixing-length variations, the role of dispersive stresses, and the effective value of c_d; and (iii) variations of z_{om} and d with λ_f, λ_p, c_d and how the results in (ii) modify them. Towards addressing these objectives, published LES runs across different arrangements of cuboids are analysed (Li et al. 2020). The arrangements are labelled as VPF (variable plan and frontal area density), VP (variable plan density), and VF (variable frontal density) and include five runs per arrangement. The values of their respective λ_f and λ_p are listed in Table 1 . These fifteen runs cover cases where both λ_f and λ_p vary individually and jointly. A schematic diagram of the LES results was shown in Li et al. (2020, Fig. 2)

The effects of λ_f, λ_p, and c_d first and foremost impact a, which in turn, uniquely determine d/h (from centroid of drag force arguments) and z_{om}/d (from velocity profile matching at $z/h = 1$). For this reason, the validity of the exponential profile (i.e. whether a exists or not) and links between a inferred from LES derived U/U_h and its relation to λ_f, λ_p, and L_c are first discussed.

Before presenting the results in subsequent sections, two limitations of the LES computed flow field and their implications for how the results are interpreted are now summarized. First, the LES used here employs a diffusive immersed boundary method, meaning that the solid/fluid boundary is not as clearly defined as in a sharp immersed-boundary-method codes. Second, the resolved and subgrid-scale turbulent kinetic energy are added to the pressure and a modified pressure is obtained by solving the Poisson equation. This second limitation precludes the determination of the pressure drag by integration over the obstacles. Previous studies using the same LES code have been evaluated with experimental and direct numerical simulation data (Li et al. 2016) for flows over staggered cubes (similar to the setup here). The first and second-order statistics within the CSL agree with the referenced data in the aforementioned study. Therefore, in the horizontally averaged momentum equation for U, at least, the dispersive fluxes (computed from three-dimensional mean velocity fields) and Reynolds stress (second-order statistics with both resolved and subgrid-scale components) can be deemed accurate based on this previous evaluation of the code. With the imposed pressure gradient, the total pressure drag for the entire urban canopy (not individual roughness elements) can still be computed as a residual term (as done here). Sensitivity tests on grid resolution have also been conducted and summarized in previous studies that generated some of the results here (Li and Bou-Zeid 2019, Appendix A). It was shown that the mean and second-order statistics have a relative error of 1.5% and 5.5% compared to the double-resolution test case.

Table 1 Summary of LES parameters and results: N_i^b is the number of nodes resolving one obstacle ($i = 1$ is x or longitudinal direction, $i = 2$ is y or lateral direction and $i = 3$ is z or vertical direction)

Case	λ_p	λ_f	N_x^b, N_y^b, N_z^b	N_x, N_y, N_z	a	d/h	z_{om}/h	β	$u_\tau/U(h)$
VPF12	0.125	0.125	8, 4, 8	192, 96, 64	0.94	0.70	0.030	0.56	0.19
VPF18	0.1875	0.1875	8, 6, 8	192, 96, 64	1.2	0.7	0.057	0.50	0.29
VPF31	0.3125	0.3125	8, 10, 8	192, 96, 64	3.13	0.81	0.058	0.51	0.46
VPF37	0.3725	0.3725	8, 12, 8	192, 96, 64	3.93	0.85	0.050	0.45	0.51
VPF43	0.4375	0.4375	8, 14, 8	192, 96, 64	5.09	0.87	0.048	0.45	0.61
VP12	0.125	0.25	4, 8, 8	192, 96, 64	1.69	0.46	0.16	0.85	0.43
VP18	0.1875	0.25	6, 8, 8	192, 96, 64	1.89	0.61	0.11	0.74	0.40
VP25	0.25	0.25	8, 8, 8	192, 96, 64	2.03	0.67	0.087	0.68	0.39
VP31	0.3125	0.25	10, 8, 8	192, 96, 64	2.62	0.79	0.061	0.64	0.38
VP43	0.4375	0.25	14, 8, 8	192, 96, 64	4.58	0.94	0.026	0.25	0.45
VF08	0.12	0.08	12, 4, 8	200, 100, 64	0.73	0.75	0.014	0.50	0.15
VF12	0.12	0.12	8, 6, 8	200, 100, 64	0.84	0.60	0.048	0.63	0.21
VF16	0.12	0.16	6, 8, 8	200, 100, 64	0.92	0.51	0.10	0.60	0.29
VF24	0.12	0.24	4, 12, 8	200, 100, 64	2.31	0.45	0.19	1.03	0.49
VF32	0.12	0.32	3, 16, 8	200, 100, 64	3.67	0.55	0.19	0.99	0.66

N_i is the total number of nodes for the entire domain in the i direction. For all cases, $N_z/N_z^b = 8$ and the grid size is uniform. The number of nodes resolving the repeating units of dimensions $D_x \times D_y$ are 32×32, 32×32 and 40×40 for VPF, VP and VF, respectively, where V is 'variable', P is 'plan' and F is 'frontal' area; and the last two digits represent the first two decimal values of λ_p or λ_f. The parameter a is the attenuation coefficient obtained by fitting the LES computed U to an exponential profile. The aerodynamic parameters d/h and z_{om}/h are both fitted from LES results in the ISL. The parameter β is determined from Eq. 28. The u_τ is determined from the constant pressure gradient imposed ($= 1\,\mathrm{m\,s^{-1}}$) for all cases. The obstacle Reynolds number defined by $u_\tau h/\nu$ is 1.19×10^6

3.1 Exponential Shape of $U(z)$

The variations in U/U_h with z/h for $0 < z/h \leq 1$ from the LES runs are first analyzed in Fig. 1. The colours for the symbols going from blue, cyan, green, yellow to orange (i.e. changing from cold to warm colours) indicate an increasing λ_p in cases VFP, VP and λ_f in case VF. The same colour scale is used throughout the rest of the analysis unless stated otherwise. The attenuation coefficient a is determined by fitting the exponential profile in all runs to regions where $U/U_h \geq 0$ (no reversed flow). The fitted values of a are found by a least-squares error minimization procedure. In this procedure, the ordinate $Y = \mathrm{In}[U(z)/U_h]$ is regressed against the abscissa $X = z/h - 1$ (for $z/h < 1$) using $Y = aX$, where the y-intercept in the regression is forced to zero. The fitted a for each run is tabulated in Table 1. For cases with high λ_p and/or λ_f, significant recirculating zones exist. For the recirculation zones, $U(z)$ in the lower part of the CSL becomes negative (i.e. separation) and the exponential profile does not apply within those zones. For $z/h \geq 0.6$, especially for VPF and VP, the fitted exponential mean velocity profile appears an acceptable descriptor of the LES runs. The computed a for most cases in VPF and all cases in VP satisfy the dense canopy criterion (i.e. $a > 1$) as shown in Table 1. In few VF cases, the resulting values of a associated with $\lambda_f \leq 0.16$ do not satisfy such criterion (i.e. $a < 1$). Also, for those cases, the LES profiles of U/U_h appear to deviate from their exponential shape. It is also verified that $h/L_s \leq 1$ in those VF cases (a point to be discussed later). The predicted attenuation coefficients a from
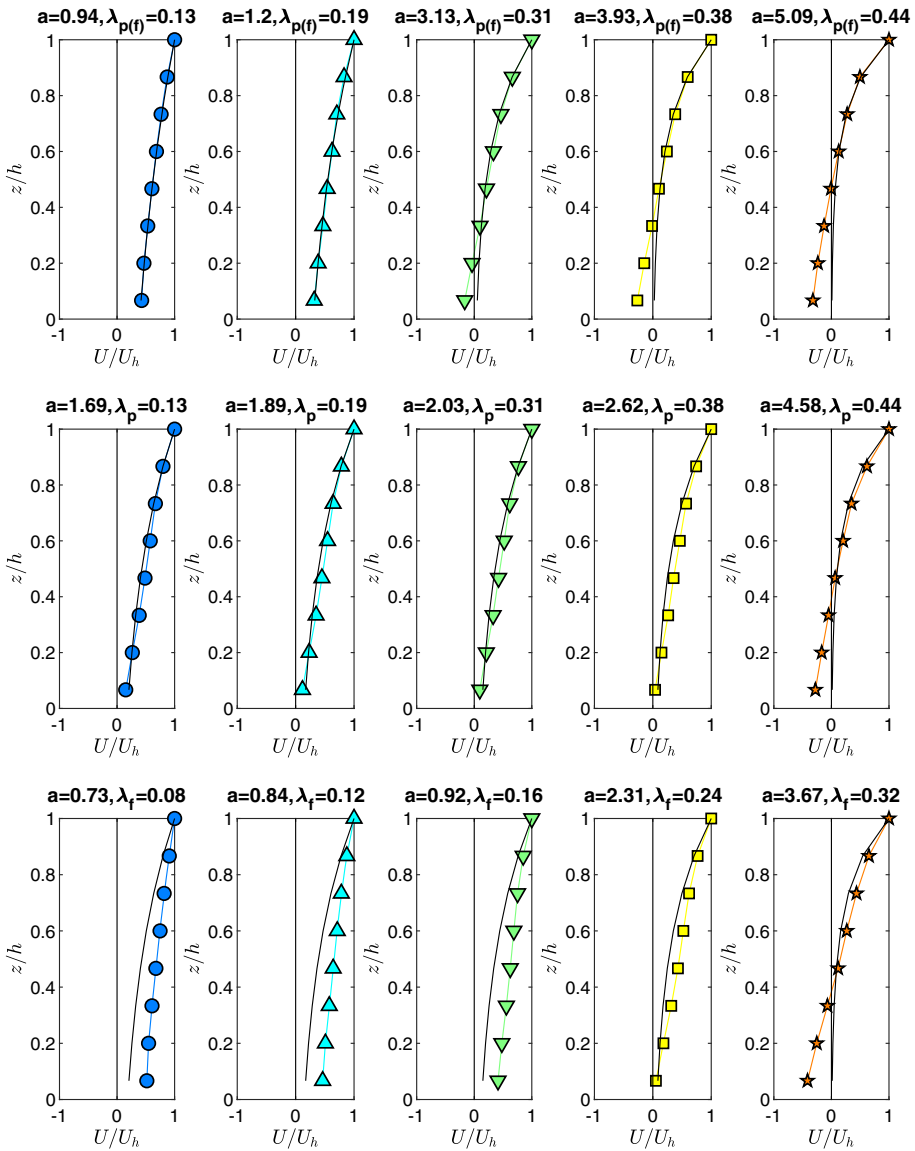
Fig. 1 The variations of normalized space–time averaged wind speed U/U_h with normalized depth z/h within the canopy for all 15 LES runs organized in the three configurations: VPF (top row, increasing $\lambda_p = \lambda_f$ from left to right), VP (middle row, increasing λ_p from left to right, $\lambda_f = 0.25$), and VF (bottom row, increasing λ_f from left to right, $\lambda_p = 0.125$). The fitted exponential profiles are shown as black solid lines. The optimized value of the attenuation coefficient a is indicated on each subplot (see Table 1). Note the values of λs shown in the figure title are rounded to only two decimal places

Eq. 14 (i.e. Eq. 15) and those fitted from the LES results (i.e. in Fig. 1) are compared in Fig. 2. The values of c_d in Fig. 2a are determined from the LES results by averaging c_d for $0.5 < z/h < 1$. The estimation of c_d from LES results will be discussed in the next section. In Fig. 2b, the calculations are repeated for $c_d = 2$, a value similar to other studies (Coceal and
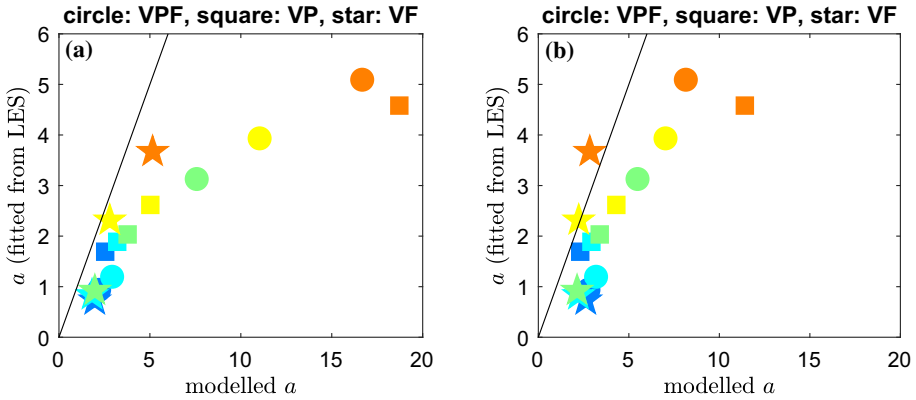
Fig. 2 Comparison between modelled attenuation coefficients a (abscissa) using Eq. 14 and inferred a from LES results (ordinate) summarized in Table 1. When computing L_c, two estimates of c_d are used. In (**a**), c_d is directly computed from the LES and then depth-averaged. In (**b**), $c_d = 2$ is assumed at all z/h
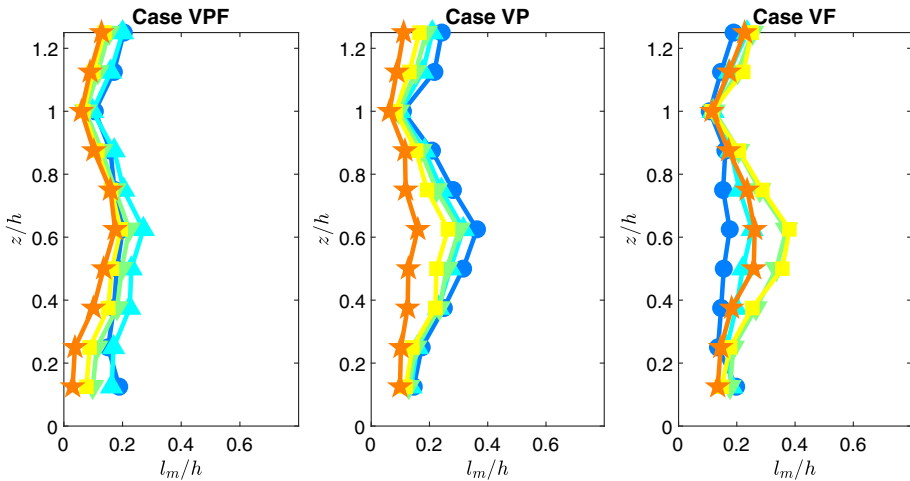
Fig. 3 The variations of LES computed normalized mixing length l_m/h with normalized height z/h for the three configurations: VPF (left), VP (middle), and VF (right)

Belcher 2004). For those cases with U/U_h that are well described by the exponential profile, the agreement between a from Eq. 14 and the fitted ones is acceptable. Equation 14 fails in cases with prominent recirculating flows as expected. The focus next is on the individual assumptions leading to Eq. 14. In particular, the LES runs are used to evaluate the l_m and L_c (i.e. Eq. 14). The assumption of dispersive stresses being negligible, which was invoked when deriving Eq. 14, is also evaluated. Neglecting dispersive stresses can be another cause for deviations between LES estimated and modelled a.

3.2 Mixing Length

The effective l_m is calculated from the LES results using Eq. 3, where τ_t is the turbulent stress that includes resolved and subgrid-scale contributions. As shown in Fig. 3, the value of $l_m(z)$
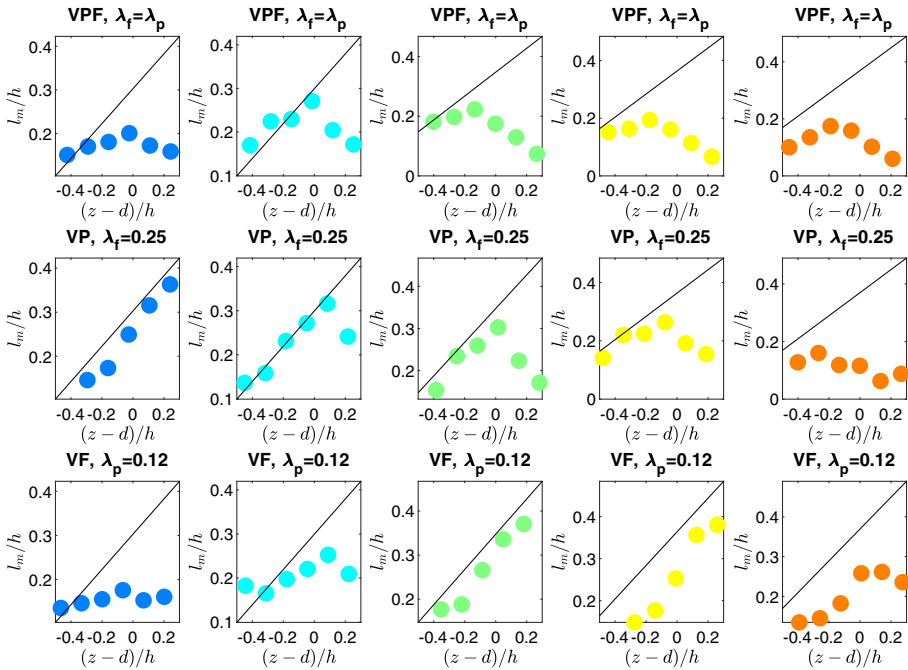
Fig. 4 Variations of l_m/h with normalized distance z/h for VPF (top), VP (middle), and VF (bottom). Black line is $\kappa z/h$ (attached eddies to the ground)

within the canopy is not constant with z across all cases and is now discussed referenced to the specific configuration (i.e. VPF, VP, and VF). In VPF (where $\lambda_p = \lambda_f$ and are varied simultaneously), there is only minor variability in $l_m(z)$ among different morphological parameters. In VP, increasing λ_p results in a higher l_m. In VF, increasing λ_f leads to a non-monotonic trend in l_m. This analysis shows that the effects of increasing urban density (i.e. λ_p) versus increasing frontal area (i.e. λ_f) on the effective eddy sizes responsible for momentum transport are likely to be different but occasionally compensating. The values of l_m peak at $0.5 < z/h < 0.7$ across almost all cases. The value $l_m(z)$ from the LES results here are broadly consistent with $l_m(z)$ synthesized from multiple studies shown in Castro (2017, Fig. 4b). Figures 5 and 4 feature $l_m(z)/h$ plotted as a function of $(z - d)/h$. They are shown in two separate figures to highlight the difference in scaling of l_m. The black solid line in Fig. 4 indicates mixing length $\kappa(z - d)$ (expected above the canopy when attached eddies dominate). Some deviations are related to the assumption that the roughness sublayer is confined to the CSL and more discussions on this point are presented later. In Fig. 5, a distance-to-the-wall scaling κz is also shown by the black dotted line. For z below where values of l_m peak, l_m roughly follows κz (i.e. attached eddies to the ground), especially for moderate values of λ_f and λ_p. In fact, the value l_m of the lower CSL below where the peak l_m value occurs appears more prevalent than a constant l_m in the upper layers of the CSL. These modifications to l_m in the lower CSL layers were considered in some models (Coceal and Belcher 2004) but not others (Yang et al. 2016).

It must be emphasized that the results here are for a canopy with a constant height. The effects of variable canopy height on the variations of l_m are to be explored in a future study.
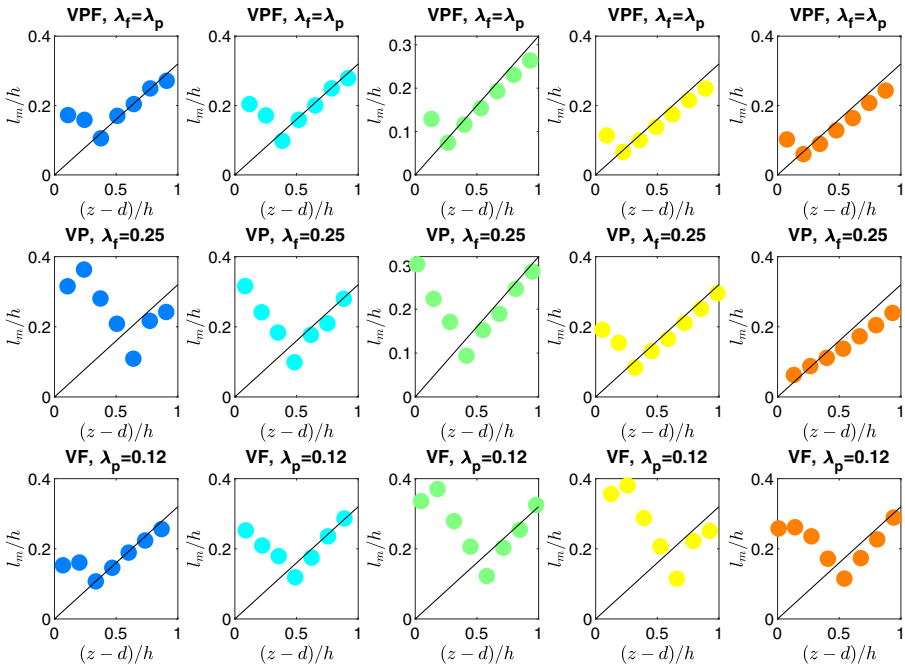
Fig. 5 Variations of l_m/h with normalized distance z/h for VPF (top), VP (middle), and VF (bottom). Black solid line is $\kappa(z-d)/h$ (attached eddies to the displacement height)

3.3 Drag Coefficient

For high Reynolds numbers flows, F_d is dominated by form drag and viscous contributions to τ are assumed to be negligible. The value of $c_d(z)$ is commonly assumed constant ($= 2$) in analytical models (Coceal and Belcher 2004; Yang et al. 2016), and this assumption is now explored using the LES results. To do so, the F_d must be first computed as a residual from Eq. 1, where $\tau = \tau_t + \tau_d$ is obtained from the LES and includes resolved and subgrid τ_t as well as τ_d. The value of $c_d(z)$ is then derived by inserting the LES computed $U(z)$ into Eq. 4 for $z/h \leq 1$. The computed c_d is subject to uncertainties in LES results, especially in the determination of F_d and c_d for the lower part of the canopy. The relative errors in first- and second-order statistics of u are below 6% (result not shown). Therefore, we choose to analyse c_d for $z/h > 1/3$ to reduce the effect of uncertainty in drag force estimation. Note that here the drag force is dominated by form drag, and the change of c_d is a result of the change in surface geometry, ultimately affecting $U(z)$. Thus, we rewrite the element Reynolds number $Re = r_b U/\nu$, where r_b is the effective dimension of the roughness element $r_b = (L_x^b L_y^b L_z^b)^{1/3}$ (i.e. geometric averaging), as $Re_\tau (r_b/h)(U(z)/u_\tau)$, where $Re_\tau = hu_\tau/\nu$ and it is fixed over all the cases studied due to the imposed constant pressure gradient. Here, we denote $Re_\tau (r_b/h)(U(z)/u_\tau)$ as Re'_τ. One can thus view the variation of $c_d(z)$ as a variation with U/u_τ, modified by changes in r_b/h over the different cases. The computed $c_d(z)$ profiles are shown in Fig. 6a as a function of Re'_τ. We emphasize here that the apparent Reynolds number dependence is not a result of a change in viscous drag as the large magnitude of Re throughout makes this fact clear. Rather, the variations are a manifestation of the change in
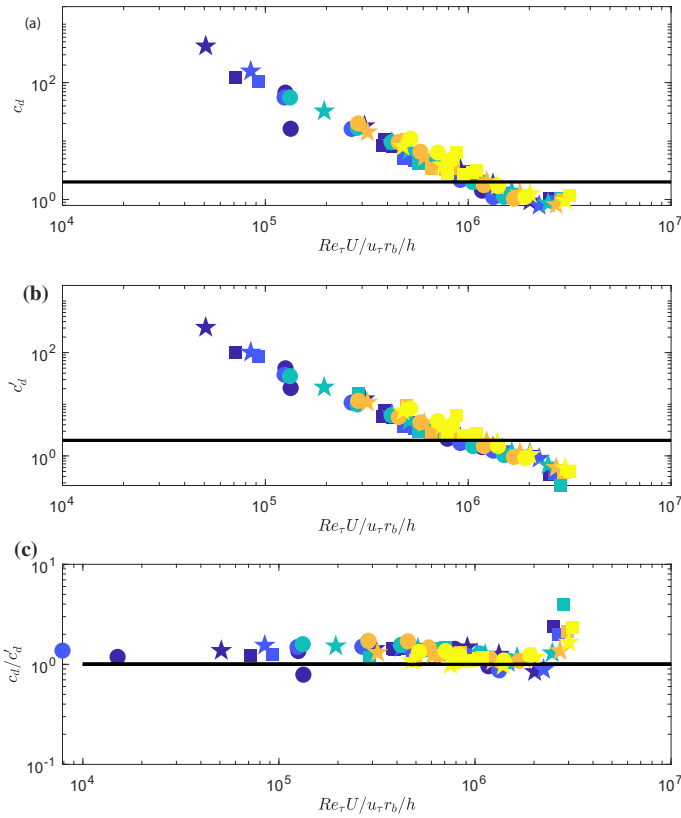
Fig. 6 **a** Variations of computed c_d with $Re_\tau(r_b/h)[U(z)/u_\tau] = Re'_\tau$ for all cases, where $r_b = (L^b_x L^b_y L^b_z)^{1/3}$. **b** Variations of c'_d with element Reynolds number $Re_\tau(r_b/h)[U(z)/u_\tau] = Re'_\tau$ for all cases. In (**a**) and (**b**), solid black horizontal line: $c_d = 2$. **c** Ratio between c_d and c'_d. Colour scale indicates normalized height z/h. Circles: VPF cases; Squares: vP cases; Stars: VF cases

z/h and different morphology of rough obstacles. For higher $Re > 10^6$, there is a tendency to converge to a constant ($c_d = 1$ instead of $c_d = 2$) as common to analytical models.

Similarly, an effective drag coefficient $c'_d(z)$ can be defined from the residual of Eq. 1 by replacing the total stress gradient $d\tau/dz$ with the turbulent stress gradient $d\tau_t/dz$. The results are shown in Fig. 6b. The main difference between $c_d(z)$ and $c_d(z)'$ is that $F_d(z)$ is computed as a residual without removing dispersive stress gradients. The ratio between c_d and c'_d is shown in Fig. 6c. For high $Re > 10^6$, c'_d appears smaller than c_d. This outcome is expected because F_d and $d\tau_d/dz$ are now acting together to balance $(dP/dx)_b$ and $d\tau_t/dz$ resulting in a reduction from c_d to c'_d. Qualitatively, a higher drag coefficient (i.e. c_d vis-a-vis c'_d) reduces L_c, which in turn, increases the attenuation coefficient a according to Eq. 14.

Figure 7 shows variations of c_d with z/h for $z/h > 1/3$. All cases show zero values at $z/h = 1$ (no drag) and increasing values of c_d with decreasing z, which are qualitatively similar to those shown in Fig. 4 in Castro (2017). Note that the cases here include high values of $\lambda_f(\lambda_p)$ [i.e. larger than 0.25, which is the densest case plotted in Fig. 4 of Castro (2017)]. It is expected that larger values of c_d are observed for these cases. The magenta filled squares indicate the laboratory results for staggered cubes of $\lambda_f, p = 0.25$ from Cheng and Castro

Fig. 7 The drag coefficient c_d versus dimensionless height z/h for all cases, where markers follow Fig. 6 and colour scale follows the colour map in Fig. 1. Magenta filled triangles indicate laboratory measurements for staggered cubes with $\lambda_f, p = 0.25$ (Cheng and Castro 2002)
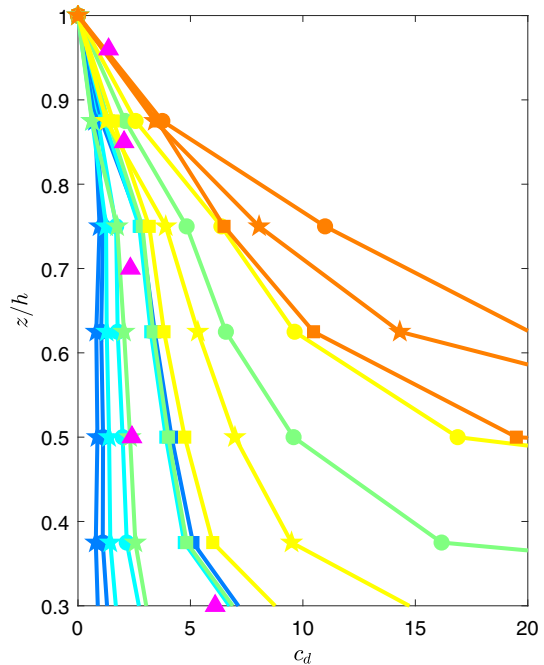

(2002), which is similar to the configuration of case VP25 in current study (i.e. shown by the green squares). Reasonable agreement between the current LES results and these laboratory measurements is noted in Fig. 7 lending some confidence to the LES estimates of c_d.

3.4 Dispersive Stresses

The normalized dispersive stresses $\langle \overline{u}''\overline{w}'' \rangle$ for all 15 cases are shown in Fig. 8. Although (as expected) dispersive stresses in the vicinity of $z/h = 0$ and $z/h = 1$ are small, they are not negligible within the CSL. For $z/h = 0.2$–0.3, dispersive fluxes for most cases are small and are broadly in agreement with prior literature (Castro 2017; Leonardi et al. 2015). The variations in dispersive stresses with height are also supported by several previous studies (Kanda et al. 2004; Leonardi and Castro 2010; Li and Bou-Zeid 2019). All cases considered here were time averaged for approximately $H/U_b = 1200$ (U_b is the bulk velocity and H is the boundary-layer height) and longer than a suggested $H/U_b = 600$ (Leonardi et al. 2015). In terms of sign, dispersive stresses derived here act in the same direction as turbulent stresses, especially towards the upper CSL layers. This finding is in contrast to vegetated canopies where dispersive stresses act in the opposite direction to turbulent stresses (Poggi and Katul 2008). Also, their contribution to the mean momentum transport in the CSL is not negligible as may be the case for dense vegetated canopies. Because $d\tau_d/dz$ and not τ_d is the significant term in the mean momentum balance, $d\tau_d/dz$ is compared against $d\tau_t/dz$. For convenience, we label $d\tau_d/dz$ as dispersive transport (in the vertical). For the upper CSL, $d\tau_d/dz$ can range from 25 to 75% of $d\tau_t/dz$ (See Fig. 9). Since negligible dispersive transport (not necessarily stress) is one of the assumptions used in deriving the exponentially attenuating $U(z)$, the omission of $d\tau_d/dz$ (often stated as $|\tau_d/\tau_t| \ll 1$) can affect a. These impacts are discussed in the following section by diagnosing how $d\tau_d/dz$ affects a either through enhanced mixing
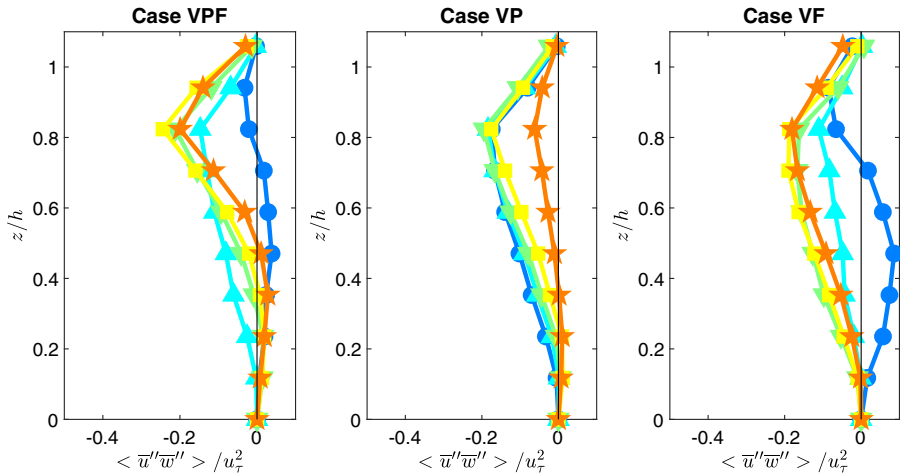
Fig. 8 Variation of normalized dispersive stresses $\langle \overline{u''}\,\overline{w''} \rangle / u_\tau^2$ with normalized height z/h for configurations VPF (left), VP (centre), and VF (right)
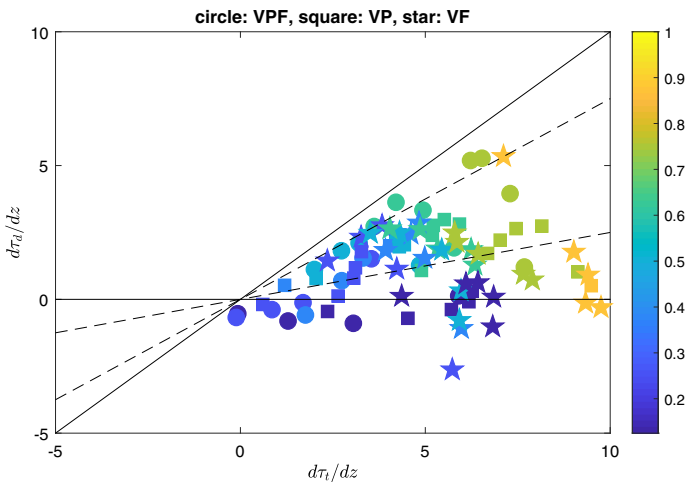
Fig. 9 Variations of $d\tau_d/dz$ with $d\tau_t/dz$. Dotted black lines denote $d\tau_d/dz = 75\%$ $d\tau_t/dz$ and $d\tau_d/dz = 25\%$ $d\tau_t/dz$. Colour scale indicates z/h

or a reduced drag coefficient (i.e. from c_d to c_d'). This diagnosis was inspired by an earlier model (Yang et al. 2016) that sought to track how the wake region behind cuboids impacts a.

4 Discussion

By assuming that neither l_m nor L_c depends on z, an exponential solution to Eq. 12 with an attenuation coefficient a is obtained. Nevertheless, analyses in this work and previous research (Castro 2017) suggest l_m and L_c vary with z/h. Such discrepancy can be viewed from the perspective of a scaling analysis and dimensional considerations, which would

suggest that a may be impacted, at minimum, by two dimensionless groups: $\Pi_1(L_c/h)$ and $\Pi_2(l_m/h)$. That is,

$$a = \frac{h}{L_s} = \left[\Pi_1\left(\frac{L_c}{h}\right)\right]\left[\Pi_2\left(\frac{l_m}{h}\right)\right]. \tag{26}$$

Under the assumption of z-independent l_m and L_c, Eq. 14 may be used to suggest $\Pi_1 = (h/L_c)^{1/3}$ whereas $\Pi_2 = (h/l_m)^{2/3}$. While h is not variable here, l_m and L_c are shown to vary across configurations, runs, and more important, with z/h. Thus, Π_1 and Π_2 are not constants. However, the LES computed U/U_h does support an exponential form for U/U_h for the majority of the runs, at least in the upper layers of the canopy ($z/h > 0.6$). These same LES runs do suggest that L_c and l_m vary with z/h. Thus, a logical question to ask is whether an inverse relation between Π_1 and Π_2 exists reflecting counteracting effects between these two dimensionless groups governing a along z/h. Such counteracting effect may explain why a is apparently constant in the fitted exponential profile. To test this hypothesis, L_c is computed using $c_d(z)$ estimated from the LES results where $L_c(z) = (2/\lambda_f)(1 - \lambda_p)[c_d(z)]^{-1}$. The two quantities $\Pi_1 = (h/L_c)^{1/3}$ and $\Pi_2 = (h/l_m)^{2/3}$ are featured in Fig. 10. The descending branch mainly corresponds to the upper CSL ($0.5 < z/h < 1$), where Π_1 monotonically decreases with Π_2, especially in cases with smaller values of λ_p and λ_f (blue, cyan, green and yellow lines and symbols within the red box). In addition, for the VF configuration with small values of λ_f, there is large scatter over a small range of $(L_c/h)^{-1/3}$. A constant a that appears to be robust to a z-dependence in c_d within the upper CSL is shown in Fig. 11 for runs without recirculation (in Case VP). Thus, for the upper CSL layers, where the exponential mean velocity profile is expected to hold, increasing L_c is partially compensated for by the decreasing l_m (See Fig. 3). Also, for most cases with smaller λ_f in VF, $a = (1/2)^{1/3}(l_m(z)/h)^{-2/3}(L_c/h)^{-1/3} < 1$ confirming that the dense canopy assumption may not hold for these cases.

Since a depends on the mixing length (derived from the τ), it may be instructive to assess whether dispersive stresses may act to increase or suppress an apparent l_m in various regions
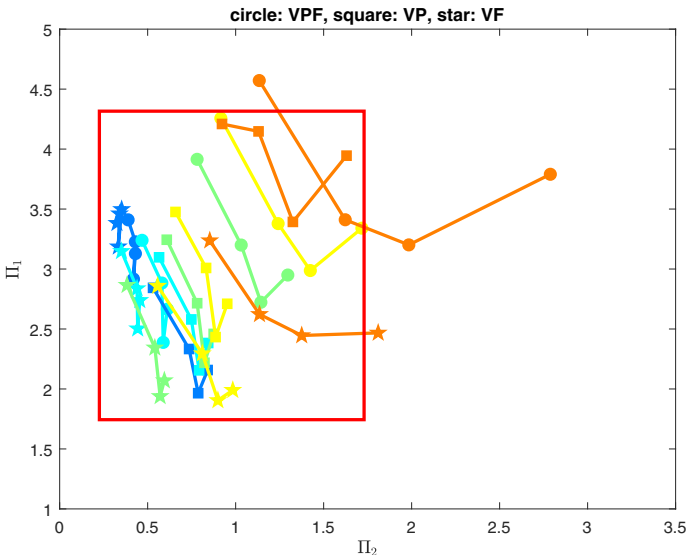

Fig. 10 The variation of $\Pi_1 = (L_c/h)^{-1/3}$ with $\Pi_2 = (l_m/h)^{-2/3}$ for all cases, where $0.5 < z/h < 1$
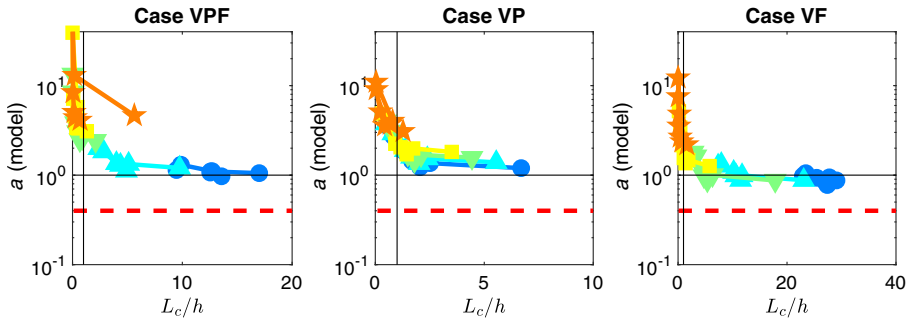
Fig. 11 The variation of the attenuation coefficient a according to Eq. 14 with L_c/h for all cases, where $0 < z/h < 1$. The black horizontal and vertical lines indicate $a = 1$ and $L_c/h = 1$, respectively. The red dotted line indicates $a = 0.4$, which is the minimum value specified in some models (Yang et al. 2016)

of the CSL. We define an effective mixing length l_m^d based on the LES computed dispersive stresses and mean velocity gradients dU/dz. These computed l_m^d are shown in Fig. 12 as a function of z/h. Compared to l_m in Fig. 3, both l_m and l_m^d show consistent variation with z/h. The peak values occur at a similar height in most cases. In addition, l_m^d can exceed l_m for smaller λ_p values for VP cases. However, for VF cases, l_m^d increases with increasing λ_f. Although invoking the mixing-length model to represent dispersive stresses must be questioned, it is only used here to assess the indirect effects of τ_d on a through enhancements in the apparent mixing length needed in Π_2. Thus, this assessment permits incorporating l_m^d into a model of a in future work.

Figure 13a features a estimated from Eq. 14 without any correction for dispersive stress, where $l_m(z)$ and $L_c(z)$ are averaged for $0 < z/h < 1$. For cases with prominent recirculating flows, the model prediction is higher than those fitted from LES results. Correcting for dispersive stress using $l_m + l_m^d$ in Eq. 14 improves the estimation of a as shown in Fig. 13b. There is underestimation of cases in VP (i.e. the squares) when correcting for the dispersive stress as a modified mixing length. Nevertheless, an alternative correction replacing c_d with
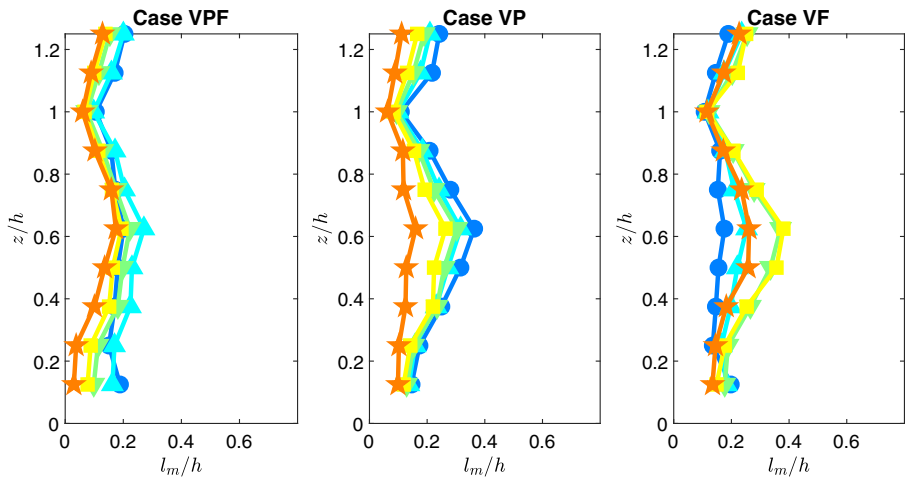

Fig. 12 Variation of l_m^d/h with normalized height z/h for the three configurations
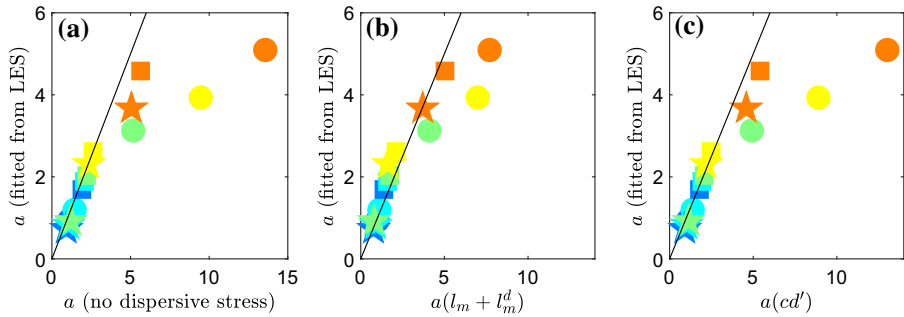
Fig. 13 Comparisons between the attenuation coefficients a fitted from LES (ordinate) and modelled from Eq. 14 (abscissa). In the model calculations, **a** shows the outcome when ignoring dispersive stresses; **b** shows the outcome of correcting for dispersive stress by including modelled l_m^d to the overall mixing length; **c** shows the outcome when correcting for dispersive stress by using c_d'

c_d' is not as effective in reducing the overestimation of a (See Fig. 13c). These results imply that for larger a that can be accompanied by strong recirculating flows in the bottom of the CSL, correcting for dispersive stress is necessary to predict a for the upper CSL. In addition, correcting for dispersive transport as a modification to a mixing length offers superior refinements to models of a when compared to using c_d' (that modifies L_c).

Up to this point, the concern was primarily the attenuation coefficient a predicted by Eq. 14. Equation 15 is now considered, where the assumption of $l_m/h = \kappa(1 - d/h)$ is made. This necessitates an evaluation of d/h. The fitted d/h values from LES (see Table 1) are compared in Fig. 14 with those computed using the centroid method (Jackson 1981) according to Eq. 19. Note that when d and z_{om} are determined from numerically simulated results, their values are affected by the von Kármán constant (Leonardi and Castro 2010) as well as the choice of the logarithmic law range. Here, $\kappa = 0.4$ is used throughout. Values of a fitted from LES results (c.f. Fig. 1 and Table 1) are used to compute d in Fig. 14a. Values of a in Fig. 14b and c correspond to those shown in Fig. 13a and b, respectively. Values of d directly fitted from LES can be subject to uncertainties in the fitting procedure and whose impacts have been analysed in previous work (Li et al. 2020, Appendix C). The centroid method in most cases overestimates d compared with those directly fitted
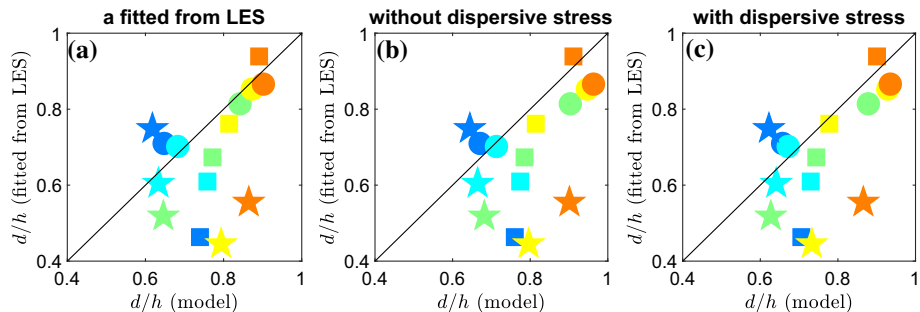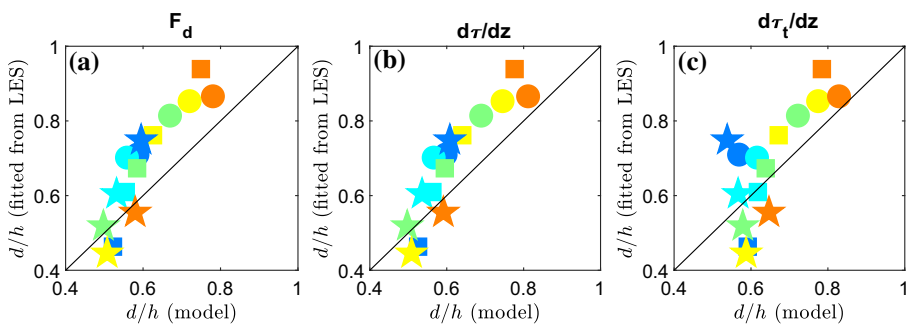

Fig. 14 Comparisons between the reference d/h obtained from fitting the log-law to U in the ISL (see Table 1) and models for d/h. **a** d/h is modelled based on Eq. 19 using attenuation coefficients a fitted from LES; **b** d/h based on Eq. 19 using a modelled by the first equality of Eq. 14 without correcting for the effect of dispersive stress on a; **c** the same as (**b**), except correcting for the effect of dispersive stress on a

from LES in Fig. 14a. In VPF, where $\lambda_{\mathrm{p}} = \lambda_{\mathrm{f}}$, the centroid method matches the results fitted from the LES. For VF (star symbols), with a relatively sparse arrangement where $\lambda_{\mathrm{p}} = 0.12$, the centroid method has the most discrepancy. In VP (square symbols) with lower λ_{p} values, although the exponential shape of U (c.f. Fig. 1 middle panels) agrees with the LES results, there are also large discrepancies in predicted values of d without accounting for dispersive stress effect in a. However, after correcting for the dispersive stress effect in a through the modified mixing length, the agreement in VP is improved. The disagreement between LES-fitted d and those computed using the centroid method in prior studies was attributed to the presence of recirculation (Kanda et al. 2004). However, in prior studies, d was found to be underestimated using the centroid method whereas the findings here suggest an overestimation. The difference between the prior studies (Kanda et al. 2004) and the present one may be due to the shear stress profile used in prior calculations. Previous studies assumed F_{d} to be the turbulent stress at the canopy top (Kanda et al. 2004). These results suggest that the presence of recirculation alone may not be the only reason for the failure of the centroid method and subsequent applications of Eq. 19 to calculate d based on a.

To probe further into the discrepancies between d/h predicted from Eq. 19 and those obtained from LES results, we note that Eq. 19 makes the additional assumption that $c_{\mathrm{d}}(z)$ is height independent. Thus, to evaluate the centroid method (i.e. Eq. 18) without this assumption (see Fig. 15a), we consider momentum sinks represented by either the drag force F_{d} or the turbulent plus dispersive stresses or the turbulent stresses only:

$$d = \frac{\int_0^h z \frac{\mathrm{d}\tau}{\mathrm{d}z}(z)\mathrm{d}z}{\int_0^h \frac{\mathrm{d}\tau}{\mathrm{d}z}(z)\mathrm{d}z}, \tag{27}$$

where we consider τ to be either the total turbulent plus dispersive stresses (see Fig. 15b) or the turbulent stresses (Fig. 15c). Note that since F_{d} is inferred as the residual from the mean momentum equation, the finite background mean pressure gradient has been included in F_{d}. Compared to d modelled using Eq. 19, using the original definition of the centroid method shows better agreement with LES results. Thus, the assumption of c_{d} being height independent can lead to biases (at least for the cases considered here). In addition, without considering the dispersive stresses acting to extract momentum, a less accurate prediction of d is also shown in Fig. 15c, further highlighting the importance of dispersive momentum transport in the CSL. As a result, the dispersive stresses can affect the ISL through their connection with d, and as we show next, z_{om}.

Fig. 15 Comparisons between the reference d/h obtained from fitting the log-law to U in the ISL and models for d/h. **a** d/h is modelled based on Eq. 18; **b** d/h is modelled based on Eq. 27; **c** the same as (**b**), except neglecting dispersive stress on in Eq. 18 (i.e. $\tau \approx \tau_{\mathrm{t}}$)
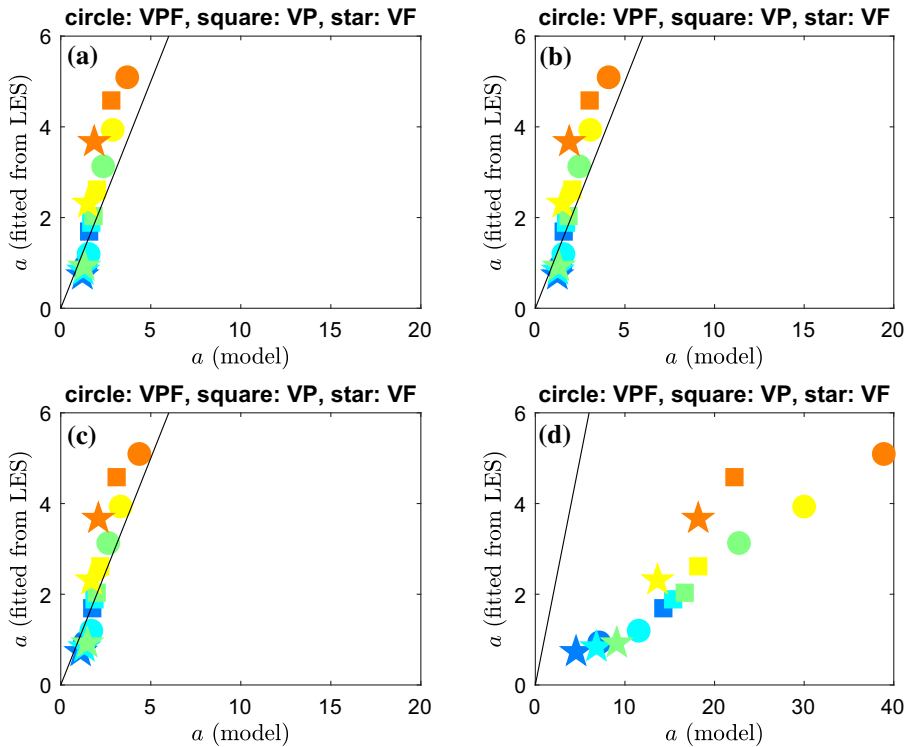
Fig. 16 Comparisons between the attenuation coefficients a fitted from LES and a computed according to Eq. 15, where d corresponds to those in Fig. 15a–c in **a–c** assuming $c_d = 2$; **d** a computed using Eq. 21

The effect of different models of d on quantifying a according to Eq. 15 shown in Fig. 16 is evaluated. Values of d from those models, shown in Fig. 15, are substituted into Eq. 15 with a constant $c_d = 2$. The comparisons are presented in Fig. 16a–c. Good agreement is found, and a similar conclusion can be drawn using c_d averaged for the upper canopy (c.f. Fig. 2a). However, a derived in Eq. 21 by assuming d follows Eq. 19 deviates significantly compared to the fitted values, as seen in Fig. 16d. This indicates that while assuming a constant mixing length of $l_m = \kappa(h - d)$ in Eq. 15 is a reasonable assumption, biases in d arising from the centroid method, where $d/h = [1 - \exp(-2a)]^{-1} - [2a]^{-1}$, dominantly contribute to the discrepancies.

The effects of d and a on the determination of z_{om} are now examined. According to Eq. 23, z_{om} depends on L_c and d or equivalently a and d. Using d fitted from the LES and L_c averaged over the upper CSL, a comparison between predictions from Eq. 23 and the reference z_{om} (shown in Table 1) is presented in Fig. 17a. The predicted values of z_{om} from Eq. 23 and those fitted from the LES results are in good agreement. The sensitivity of the modelled z_{om} to the inference of d is now explored. Using the centroid method in Eq. 27 and L_c averaged over the upper CSL, z_{om} in Fig. 17 also shows acceptable agreement with the reference z_{om}. By modelling a from Eq. 21 and using the same d as that in Fig. 17b, there are some discrepancies between the predicted z_{om} and the reference z_{om} (see Fig. 17c). These discrepancies occur despite significant biases in a existing when using Eq. 21 as seen in Fig. 16d. Combining a from Eq. 21 and d from Eq. 19, values of z_{om} in Fig. 17d are
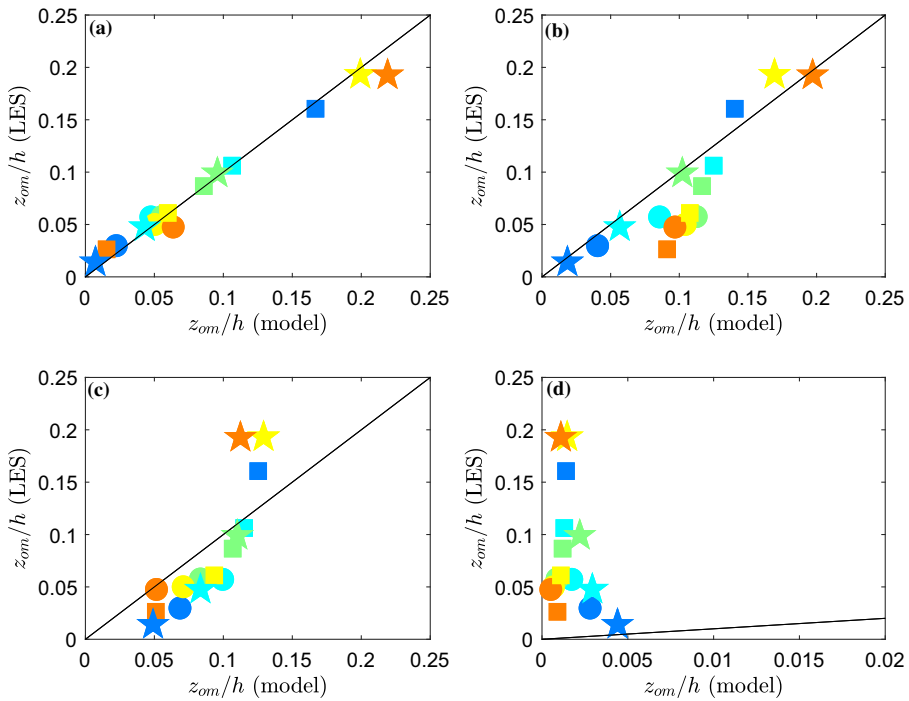
Fig. 17 A comparison between the reference z_{om}/h obtained from fitting LES computed U to the log-profile in the ISL (see Table 1) and z_{om} based on Eq. 23. **a** z_{om} based on Eq. 23 with d obtained from the fitted log-profile; **b** z_{om} based on the second equality in Eq. 23 with d shown in Fig. 15b; **c** z_{om} based on the first equality in Eq. 23 with d computed according to those in Fig. 15b and a according to Eq. 21 as shown in Fig. 16b; **d** z_{om} based on the first equality in Eq. 23 with d computed using Eq. 19 and a according to Eq. 21 as shown in Fig. 16b

significantly underestimated. To be clear, such underestimation is caused by inaccurate d estimates arising from Eq. 19, which assumes a height-independent $c_d(z)$ when using the centroid method. This also indicates that z_{om} is more sensitive to uncertainties in d than to a (or L_c).

Another factor that has been overlooked up to this point is the existence of a RSL above $z/h = 1$. The impact of this factor is now considered from the smoothness condition imposed on U at $z/h = 1$. Because a smoothness condition is formulated based on matching gradients instead of states at a single point ($z/h = 1$), it can be used as a sensitive marker to any modulations by a finite RSL above $z/h = 1$. As earlier noted, the smoothness condition on U imposed at $z/h = 1$ leads to a unique relation between u_τ/U_h, a, and d/h. Equation 24 can be directly tested with d/h obtained from the LES fit, a obtained from the fit to the LES velocity in the CSL, and u_τ/U_h directly computed by the LES (see Table 1). The assumption of zero-thickness RSL above $z/h = 1$ leads to a $\beta = 1$ (i.e. only attached eddies contribute to momentum flux at $z/h = 1$).

Figure 18 suggests that when $a > 1$, β is reasonably constrained to a restricted range ($\beta = 0.6-0.8$) and this estimate is commensurate with vegetated canopy values $\beta = 0.7$. When $\beta \neq 1$, all prior occurrences of κz_d can be replaced with $\kappa z_d/\beta$. These revisions result
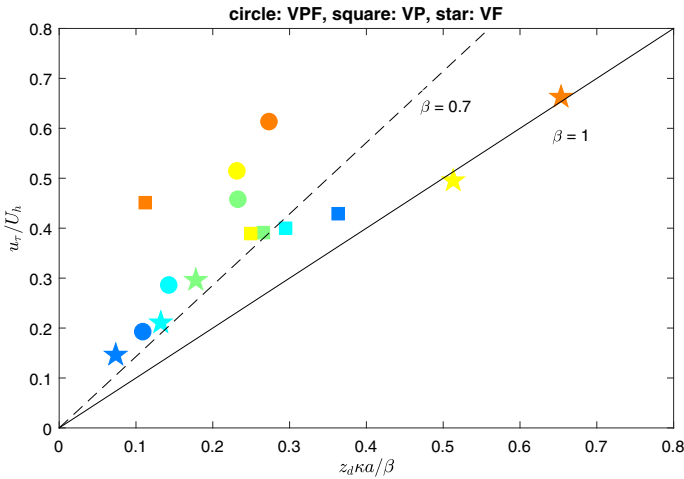
Fig. 18 Variations of LES computed u_τ/U_h versus $z_d\kappa a\beta^{-1}$ according to the first equality in Eq. 28. Solid black line indicates $\beta = 1$ (RSL coincides with the CSL); dotted black line indicates $\beta = 0.7$ (i.e. β commensurate with vegetated canopy flows)

in

$$\frac{u_\tau}{U_h} = z_d\,\frac{\kappa}{\beta}\,a \approx \frac{\kappa}{2}\frac{1}{\beta}, \tag{28}$$

and

$$a = \left[\frac{c_d\lambda_f}{1-\lambda_p}\right]^{1/3}\left[\frac{\kappa}{\beta}(z_d)\right]^{-2/3} = 4\beta^2\left(\frac{c_d}{\kappa^2}\right)\frac{\lambda_f}{1-\lambda_p}. \tag{29}$$

While a is impacted by $\beta \neq 1$, β does not alter the relation between z_{om}, a, and z_d. Likewise, $z_d \approx (1/2)a^{-1}$ from the centroid method is not impacted by β and d only sees modifications arising from β through a.

5 Conclusions

In earlier analytical models where l_m and c_d were set constant and τ_d ignored, the working assumption was that the exponential mean velocity profile along with a well-defined attenuation coefficient a independent of z/h can be derived for the urban canopy sublayer (Yang et al. 2016). Thus, the focus of prior models was on how persistent spatial patterns in U arising from the wake region behind cuboids impact a. Here, a different route is taken. The direct impact on a of dispersive terms, variable c_d and l_m are diagnosed within a one-dimensional mean momentum equation framework. These effects are then propagated to variations in aerodynamic parameters (i.e. d and z_{om}) that are formulated as a function of a. The following can be concluded:

(i) For dense urban canopies, the shape of $U(z)$ is reasonably exponential for the upper layers of the canopy ($z/h > 0.6$) allowing an attenuation coefficient ($a \geq 1$) to be defined. The λ_p and λ_f ranges here exceed those of earlier studies (Yang et al. 2016). Thus, when the present and prior LES studies are taken together, the exponential profile for U appears to be a robust representation for the upper layers of the canopy but not the entire canopy layer. For applications in numerical weather prediction in urban areas,

if the canopy wind speed is of interest, the exponential wind profile with an appropriate attenuation coefficient based on parametrizations of z_{om} and d can be reasonable (Li et al. 2021).

(ii) The finding in (i) need not necessarily imply that l_m and c_d are constant independent of z/h, or that τ_d can be ignored relative to τ_t. The work here shows that l_m and c_d do vary with z/h, but some compensatory effects on the attenuation coefficient a arise between l_m and L_c due to dispersive stresses. To a leading order, dispersive transport increases the overall apparent mixing length but increases c_d leading to a reduction in L_c. These two effects act to ameliorate variations in a with z/h.

(iii) The existence of recirculation zones at the lower layers of the CSL appears to coincide with high d/h when d is inferred from the LES computed velocity profile in the ISL. By and large, centroid methods acting on F_d or $d\tau_t/dz$ result in higher d/h predictions compared to what the flow experiences in the ISL. This finding is opposite to what was reported in earlier studies for reasons highlighted in the discussion. The z_{om} models are far more sensitive to discrepancies in d/h than L_c. The finite thickness of the RSL above the CSL leads to modifications to a by increasing the effective von Kármán constant. These modifications must be accounted for when estimating z_{om} and d from a.

References

Belcher S, Jerram N, Hunt J (2003) Adjustment of a turbulent boundary layer to a canopy of roughness elements. J Fluid Mech 488:369–398

Blunn LP, Coceal O, Nazarian N, Barlow JF, Plant RS, Bohnenstengel SI, Lean HW (2022) Turbulence Characteristics Across a Range of Idealized Urban Canopy Geometries. Boundary-Layer Meteorol 182:275–307. https://doi.org/10.1007/s10546-021-00658-6

Böhm M, Finnigan JJ, Raupach MR, Hughes D (2013) Turbulence structure within and above a canopy of bluff elements. Boundary-Layer Meteorol 146(3):393–419

Britter R, Hanna S (2003) Flow and dispersion in urban areas. Annu Rev Fluid Mech 35(1):469–496

Castro IP (2017) Are urban-canopy velocity profiles exponential? Boundary-Layer Meteorol 164(3):337–351

Cheng H, Castro IP (2002) Near wall flow over urban-like roughness. Boundary-Layer Meteorol 104(2):229–259

Christen A, Rotach MW, Vogt R (2009) The budget of turbulent kinetic energy in the urban roughness sublayer. Boundary-Layer Meteorol 131(2):193–222

Coceal O, Belcher S (2004) A canopy model of mean winds through urban areas. Q J R Meteorol Soc 130(599):1349–1372

Coceal O, Thomas TG, Castro IP, Belcher SE (2006) Mean flow and turbulence statistics over groups of urban-like cubical obstacles. Boundary-Layer Meteorol 121(3):491–519

Fernando HJ, Zajic D, Di Sabatino S, Dimitrova R, Hedquist B, Dallman A (2010) Flow, turbulence, and pollutant dispersion in urban atmospheres. Phys Fluids 22(5):051301

Finnigan J (2000) Turbulence in plant canopies. Annu Rev Fluid Mech 32(1):519

Finnigan J, Belcher S (2004) Flow over a hill covered with a plant canopy. Q J R Meteorol Soc 130(596):1–29

Giometto M, Christen A, Meneveau C, Fang J, Krafczyk M, Parlange M (2016) Spatial characteristics of roughness sublayer mean flow and turbulence over a realistic urban surface. Boundary-Layer Meteorol 160(3):425–452

Grimmond C (2006) Progress in measuring and observing the urban atmosphere. Theor Appl Climatol 84(1):3–22

Grimmond C, Oke TR (1999) Aerodynamic properties of urban areas derived from analysis of surface form. J Appl Meteorol 38(9):1262–1292

Inoue E (1963) On the turbulent structure of airflow within. J Meteorol Soc Jpn 41(6):317–326

Jackson PS (1981) On the displacement height in the logarithmic velocity profile. J Fluid Mech 111(-1):15

Juang JY, Katul GG, Siqueira MB, Stoy PC, McCarthy HR (2008) Investigating a hierarchy of Eulerian closure models for scalar transfer inside forested canopies. Boundary-Layer Meteorol 128(1):1–32

Kanda M, Moriwaki R, Kasamatsu F (2004) Large-eddy simulation of turbulent organized structures within and above explicitly resolved cube arrays. Boundary-Layer Meteorol 112(2):343–368

Kanda M, Inagaki A, Miyamoto T, Gryschka M, Raasch S (2013) A new aerodynamic parametrization for real urban surfaces. Boundary-Layer Meteorol 148(2):357–377

Katul GG, Mahrt L, Poggi D, Sanz C (2004) One-and two-equation models for canopy turbulence. Bound-Layer Meteorol 113(1):81–109

Leonardi S, Castro IP (2010) Channel flow over large cube roughness: a direct numerical simulation study. J Fluid Mech 651:519–539

Leonardi S, Orlandi P, Djenidi L, Antonia RA (2015) Heat transfer in a turbulent channel flow with square bars or circular rods on one wall. J Fluid Mech 776:512–530

Li Q, Bou-Zeid E (2019) Contrasts between momentum and scalar transport over very rough surfaces. J Fluid Mech 880:32–58

Li Q, Bou-Zeid E, Anderson W (2016) The impact and treatment of the Gibbs phenomenon in immersed boundary method simulations of momentum and scalar transport. J Comput Phys 310:237–251

Li Q, Bou-Zeid E, Grimmond S, Zilitinkevich S, Katul G (2020) Revisiting the relation between momentum and scalar roughness lengths of urban surfaces. Q J R Meteorol Soc 146(732):3144–3164

Li Q, Yang J, Yang L (2021) Impact of urban roughness representation on regional hydrometeorology: an idealized study. J Geophys Res Atmos 126(4):e2020JD033812

Macdonald RW, Griffiths RF, Hall DJ (1998) An improved method for the estimation of surface roughness of obstacle arrays. Atmos Environ 32(11):1857–1864

Martilli A, Clappier A, Rotach MW (2002) An urban surface exchange parameterisation for mesoscale models. Boundary-Layer Meteorol 104(2):261–304

Moriwaki R, Kanda M (2006) Local and global similarity in turbulent transfer of heat, water vapour, and CO_2 in the dynamic convective sublayer over a suburban area. Boundary-Layer Meteorol 120(1):163–179

Nazarian N, Krayenhoff ES, Martilli A (2020) A one-dimensional model of turbulent flow through "urban" canopies (mlucm v2. 0): updates based on large-eddy simulation. Geosci Model Dev 13(3):937–953

Nepf HM, Vivoni E (2000) Flow structure in depth-limited, vegetated flow. J Geophys Res Oceans 105(C12):28547–28557

Poggi D, Katul GG (2008) The effect of canopy roughness density on the constitutive components of the dispersive stresses. Exp Fluids 45(1):111–121

Poggi D, Katul G, Albertson J (2004) Momentum transfer and turbulent kinetic energy budgets within a dense model canopy. Boundary-Layer Meteorol 111(3):589–614

Poggi D, Katul G, Albertson J (2004) A note on the contribution of dispersive fluxes to momentum transfer within canopies. Boundary-Layer Meteorol 111(3):615–621

Poggi D, Porporato A, Ridolfi L, Albertson J, Katul G (2004) The effect of vegetation density on canopy sub-layer turbulence. Boundary-Layer Meteorol 111(3):565–587

Poggi D, Krug C, Katul GG (2009) Hydraulic resistance of submerged rigid vegetation derived from first-order closure models. Water Resour Res 45:W10442

Pope SB (2000) Turbulent flows. Cambridge University Press, Cambridge

Raupach MR (1981) Conditional statistics of Reynolds stress in rough-wall and smooth-wall turbulent boundary layers. J Fluid Mech 108(-1):363–382

Raupach MR, Finnigan JJ, Brunei Y (1996) Coherent eddies and turbulence in vegetation canopies: the mixing-layer analogy. Boundary-Layer Meteorol 78(3–4):351–382

Rotach MW (1999) On the influence of the urban roughness sublayer on turbulence and dispersion. Atmos Environ 33(24–25):4001–4008

Schmid MF, Lawrence GA, Parlange MB, Giometto MG (2019) Volume averaging for urban canopies. Boundary-Layer Meteorol 173(3):349–372

Xu H, Altland S, Yang X, Kunz R (2021) Flow over closely packed cubical roughness. J Fluid Mech 920:A37. https://doi.org/10.1017/jfm.2021.456

Yang XIA, Sadique J, Mittal R, Meneveau C (2016) Exponential roughness layer and analytical model for turbulent boundary layer flow over rectangular-prism roughness elements. J Fluid Mech 789:127

Yoshida T, Takemi T, Horiguchi M (2018) Large-eddy-simulation study of the effects of building-height variability on turbulent flows over an actual urban area. Boundary-Layer Meteorol 168(1):127–153